



Sensing mode coupling analysis for dual-mass MEMS gyroscope and bandwidth expansion within wide-temperature range



Huiliang Cao^{a,b}, Hongsheng Li^c, Xingling Shao^{a,b}, Zhiyu Liu^{a,b}, Zhiwei Kou^{a,b}, Yanhu Shan^{a,b}, Yunbo Shi^{a,b}, Chong Shen^{a,b,*}, Jun Liu^{a,b,*}

^a Key Laboratory of Instrumentation Science & Dynamic Measurement, Ministry of Education, North University of China, Tai Yuan 030051, China

^b Science and Technology on Electronic Test & Measurement Laboratory, North University of China, Tai Yuan 030051, China

^c School of Instrument Science and Engineering, Southeast University, Nanjing 210096, China

ARTICLE INFO

Article history:

Received 13 December 2016

Received in revised form 30 April 2017

Accepted 4 May 2017

Available online 18 May 2017

Keywords:

Dual-mass MEMS gyroscope

Sensing mode mechanical superposition

Force-feedback loop

Bandwidth expanding

Wide-temperature range

ABSTRACT

This paper presents the bandwidth expanding method with wide-temperature range for sense mode coupling dual-mass MEMS gyro. The real sensing mode of the gyroscope is analyzed to be the superposition of in-phase and anti-phase sensing modes. The mechanical sensitivity and bandwidth of the gyroscope structure are conflicted with each other and both governed by the frequency difference between sensing and drive modes (min $\{\Delta\omega_1, \Delta\omega_2\}$). The sensing mode force rebalancing combs stimulation method (FRCSM) is presented to simulate the Coriolis force, and based on this method, the gyro's dynamic characteristics are tested. The sensing closed-loop controller is achieved by operational amplifier based on phase lead method, which enable the magnitude margin and phase margin of the system to reach 7.21 dB and 34.6° respectively, and the closed-loop system also expands gyro bandwidth from 13 Hz (sensing open-loop) to 102 Hz (sensing closed-loop). What's more, the turntable test results show that the sensing closed-loop works stably in wide-temperature range (from −40 °C to 60 °C) and the bandwidth values are 107 Hz @−40 °C and 97 Hz @60 °C. The results indicate that the higher temperature causes lower bandwidth, and verify the simulation results are 103 Hz @−40 °C and 98.2 Hz @60 °C. The new bottleneck of the closed loop bandwidth is the valley generated by conjugate zeros, which is formed by superposition of sensing modes.

© 2017 Elsevier Ltd. All rights reserved.

1. Introduction

THE MEMS gyroscopes are utilized in more and more application areas with their precision developed in these years. The application areas cover inertial navigation, automotive safety, industrial controlling and consumer electronics [1,2]. High precision MEMS gyros are reported in literatures, and the bias drift parameters are even better than the Tactical Grade requirement. But the bandwidth performance always restrains the MEMS gyro application (100 Hz bandwidth is required in both Tactical and Inertial Grade) [3]. For most linear vibrating MEMS gyro, the mechanical sensitivity is determined by the difference between drive and sensing modes' resonant frequencies Δf . It means smaller difference achieves higher mechanical sensitivity (such as higher scale factor, higher resolution and smaller output noise) [4]. It is also proved that

* Corresponding authors at: Science and Technology on Electronic Test & Measurement Laboratory, North University of China, Tai Yuan 030051, China.
E-mail addresses: shenchong@nuc.edu.cn (C. Shen), liuj@nuc.edu.cn (J. Liu).

the mechanical bandwidth of the gyro is about $0.54\Delta f$ [5], so smaller Δf causes worse bandwidth characteristic. Some works employ mode-matching technology to make $\Delta f \approx 0$ Hz, and the best mechanical sensitivity can be acquired but bandwidth is sacrificed [6]. It seems like that the bargain should be made between mechanical sensitivity and bandwidth in sensing open-loop. So the sensing closed-loop is required to improve MEMS gyro dynamic characteristics and bandwidth. The work in [7] employs a $\Sigma\Delta$ closed-loop to reduce the frequency difference between the drive and sensing mode to less than 50 Hz. The research in work [8] utilizes PI controlling technology to make Δf tunable, and the bandwidth is optimized to 50 Hz. The sensing closed-loop for single mass MEMS gyroscope based on AGC technology is proposed in paper [9]. The force rebalance controller extends the bandwidth, but it only contains a pure integral section which makes sensing closed-loop with high Q value structure unstable. The bandwidth for another single mass MEMS gyroscope is introduced in work [10], the bandwidth is improved from 30 Hz to 98 Hz with notch filter and lead-lag compensator. The notch filter is designed for the “peak response” caused by the conjugate complex poles at Δf . But the resonant frequencies of the drive and sensing modes usually drift with temperature [11], so the notch filter method cannot satisfy the temperature-changing environment. The work in [12] proposes a method to avoid problems caused by notch filter and expands the bandwidth from 2.3 Hz to 94.8 Hz. However, its left and right sensing modes are not coupled, and the bandwidth is only determined by the low pass filter (different with left and right sensing modes coupled structure). Its dual-mass structure can be considered as two independent gyroscopes with different Δf s, and two sensing loops should be designed separately to expand the bandwidth. The left and right sensing modes coupled structures are investigated in [13–15]. The work in [13] illustrates the vibration characteristics of dual-mass and spring structure. The work in paper [14] analyzes the energy of gyroscope under in-phase and anti-phase modes. And literature [15] proposes the real working sensing mode of gyroscope is formed by sensing in-phase and anti-phase modes. However, these works do not focus on the bandwidth method of this kind sensing loop. The gyro bandwidth optimized by mechanical method is proposed in paper [16], but the bandwidth varies with the temperature. Literature [17] employs eight drive mode units to form a drive band (not a single frequency). It provides a high mechanical sensitivity band for the gyroscope, but the bandwidth is determined by sensing mode frequency. And the phase margin of the closed loop is difficult to design. In work [18], the bandwidth estimation methods of MEMS gyroscope in open loop and closed loop are proposed, but the bandwidth expanding method is not discussed clearly. The precise test method of bandwidth is introduced in work [19]. The method uses vibration velocity of virtual drive mode multiplied by virtual angular rate to generate Coriolis force, and substitutes angular turntable. The vibration velocity of drive mode is produced by signal source, not by drive mode, which ignores the frequency drift of drive mode and the mechanical coupling between drive and sensing mode [20,21].

The work in this paper focuses on the bandwidth characteristics of dual-mass linear vibration MEMS gyroscope (with left and right sensing structure coupling). Also, this paper finds an effective way to break the conflict between mechanical sensitivity and bandwidth. Furthermore, the force rebalancing combs stimulation method (FRCSM) is proposed to verify the method. This paper is organized as following: Section 2 investigates the real working model of dual-mass structure sensing mode and introduces the FRCSM. In Section 3, sensing closed loop and bandwidth expanding method based on proportional integral phase lead controller (PIPLC) are described, including the parameters design and system simulation. Then, the gyro monitoring system and experimental results are given in Section 4. The results discussion and concluding remarks are shown in Section 5.

2. Real working model of sensing mode coupling gyroscope

2.1. Sensing mode analysis

The dual-mass MEMS gyroscope researched in this paper is shown in Fig. 1 [22]. The drive mode of the structure bases on tuning fork theory. The left and right masses are coupled by connect U-shaped spring, when two sensing masses are coupled by the x axis warp of drive springs. The mode analyses of the first four order modes are shown in Fig. 2 [11].

The first order mode is drive in-phase mode, the left and right masses together with drive frames vibrate towards same direction along drive axis (x direction in Fig. 1), as shown in Fig. 2 (a).

The second and third order modes are sensing in-phase and anti-phase modes, as shown in Fig. 2(b) and (c). The left and right masses together with sense frames vibrate in same and inverse directions along sensing axis (y direction in Fig. 1) respectively. And sensing anti-phase mode is the expected working mode.

Drive anti-phase mode is the fourth order, in which mode, the left and right masses move inverse directions along drive axis as Fig. 2(d) shows. The drive anti-phase is another expected working mode.

So, left and right masses both have two degrees of freedom (in x and y direction). Drive frame has one degrees of freedom (in x direction) and sense frame has one degrees of freedom (in y direction). The angular input axis is z axis in Fig. 1.

Due to large difference (>1000 Hz) between the in-phase (the 1st mode) and anti-phase drive modes frequencies, the quality factor of drive anti-phase mode is $Q_{x2} > 2000$ and the stimulating method of the drive mode. The real working drive mode is considered to be pure anti-phase drive mode (the 4th mode). Considering the real working sensing mode is formed by 2nd and 3rd modes, the motion equation of gyroscope structure can be expressed as (ideal condition) [1]:

$$m\ddot{\mathbf{D}} + c\dot{\mathbf{D}} + k\mathbf{D} = \mathbf{F} \quad (1)$$

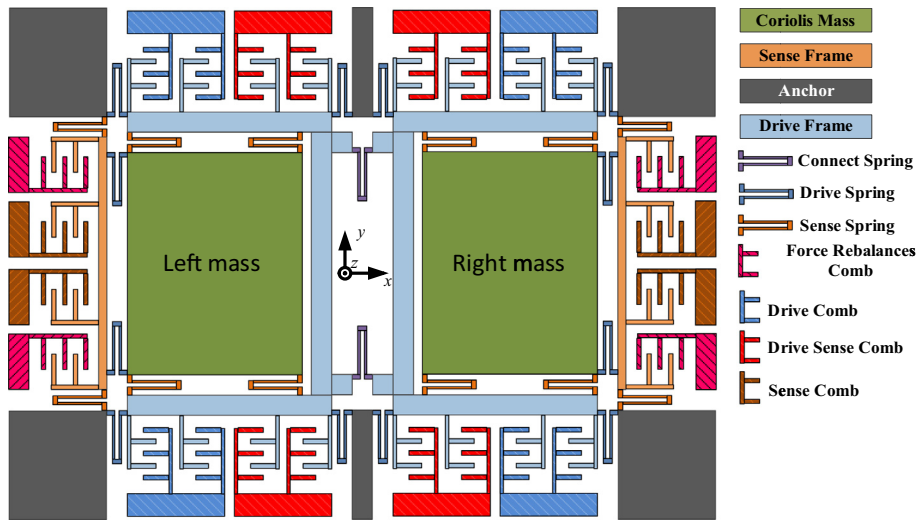


Fig. 1. Mechanical model of decoupled dual-mass gyro structure.

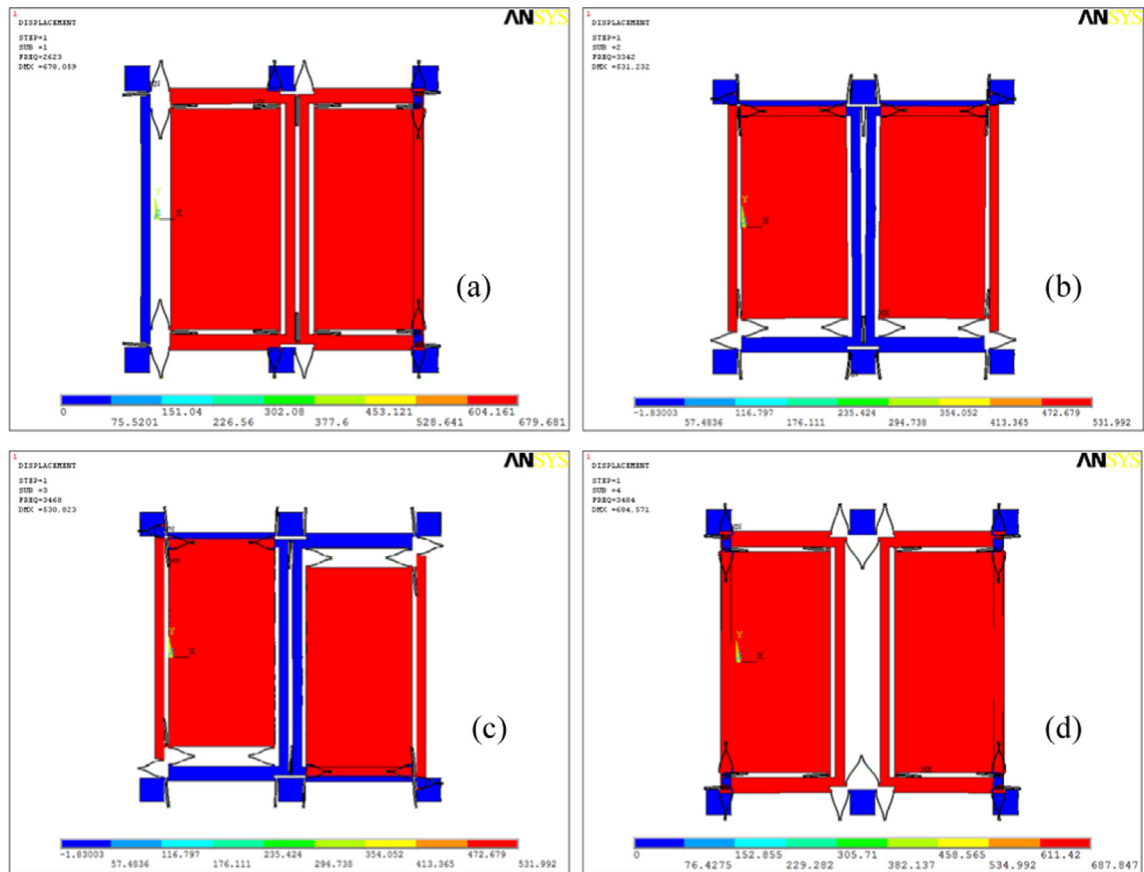


Fig. 2. (a) Drive in phase mode (1st mode) with frequency $\omega_{x1} = 2623 \times 2\pi$ rad/s; (b) Sensing in phase mode (2nd mode) with frequency $\omega_{y1} = 3342 \times 2\pi$ rad/s; (c) Sensing anti phase mode (3rd mode) with frequency $\omega_{y2} = 3468 \times 2\pi$ rad/s; (d) Drive anti phase mode (4th mode) with frequency $\omega_{x2} = 3484 \times 2\pi$ rad/s.

where $\mathbf{m} = \begin{bmatrix} m_x \\ m_y \end{bmatrix}$, $\mathbf{D} = \begin{bmatrix} x \\ y_1 \\ y_2 \end{bmatrix}$, $\mathbf{k} = \begin{bmatrix} \omega_{x2}^2 m_x & 0 & 0 \\ 0 & \omega_{y1}^2 m_y & 0 \\ 0 & 0 & \omega_{y2}^2 m_y \end{bmatrix}$, $\mathbf{c} = \begin{bmatrix} \frac{\omega_{x2} m_x}{Q_{x2}} & 0 & 0 \\ 0 & \frac{\omega_{y1} m_y}{Q_{y1}} & 0 \\ 0 & 0 & \frac{\omega_{y2} m_y}{Q_{y2}} \end{bmatrix}$, $\mathbf{F} = \begin{bmatrix} F_d \sin(\omega_d t) \\ -2m_c \Omega_z \dot{x} \\ -2m_c \Omega_z \dot{x} \end{bmatrix}$ are the mass, displacement, stiffness, damping and external force matrix respectively; m_x is equivalent mass of drive mode; x is displacement of drive mode; y_1 and y_2 are displacements of sensing in-phase and anti-phase modes respectively; Q_{y1} and Q_{y2} are quality factors; Ω_z is angular rate input; sensing mode mass m_y approximates to Coriolis mass m_c ; F_d and ω_d are stimulating magnitude and frequency of drive mode; sensing mode displacement $y = y_1 + y_2$, and we get:

$$x(t) = \frac{F_d/m_x}{\sqrt{(\omega_{x2}^2 - \omega_d^2)^2 + \omega_{x2}^2 \omega_d^2 / Q_{x2}^2}} \sin(\omega_d t + \varphi_{x2}) + \frac{F_d \omega_{x2} \omega_d / m_x Q_{x2}}{(\omega_{x2}^2 - \omega_d^2)^2 + \omega_{x2}^2 \omega_d^2 / Q_{x2}^2} e^{-\frac{\omega_{x2}}{2Q_{x2}} t} \cos\left(\sqrt{1 - 1/4Q_{x2}^2} \omega_{x2} t\right) + \frac{F_d \omega_d (\omega_{x2}^2 / Q_{x2}^2 + \omega_d^2 - \omega_{x2}^2) / m_x}{\omega_{x2} \sqrt{1 - 1/4Q_{x2}^2} [(\omega_{x2}^2 - \omega_d^2)^2 + \omega_{x2}^2 \omega_d^2 / Q_{x2}^2]} e^{-\frac{\omega_{x2}}{2Q_{x2}} t} \sin\left(\sqrt{1 - 1/4Q_{x2}^2} \omega_{x2} t\right) \quad (2)$$

$$y_{1,2}(t) = \frac{F_c}{\sqrt{(\omega_{y1,2}^2 - \omega_d^2)^2 + \omega_{y1,2}^2 \omega_d^2 / Q_{y1,2}^2}} \sin\left(\omega_d t + \varphi_{x2} + \frac{\pi}{2} + \varphi_{y1,2}\right) - \frac{F_c [\omega_{y1,2} \omega_d \sin \varphi_{x2} / Q_{y1,2} + (\omega_{y1,2}^2 - \omega_d^2) \cos \varphi_{x2}]}{(\omega_{y1,2}^2 - \omega_d^2)^2 + \omega_{y1,2}^2 \omega_d^2 / Q_{y1,2}^2} e^{-\frac{\omega_{y1,2}}{2Q_{y1,2}} t} \cos\left(\sqrt{1 - 1/4Q_{y1,2}^2} \omega_{y1,2} t\right) + \frac{F_c [\omega_{y1,2} (\omega_{y1,2}^2 - 3\omega_d^2) \cos \varphi_{x2} / (2Q_{y1,2}) + \omega_d (\omega_{y1,2}^2 / (2Q_{y1,2}^2) + \omega_{y1,2}^2 - \omega_d^2) \sin \varphi_{x2}]}{\omega_{y1,2} \sqrt{1 - 1/4Q_{y1,2}^2} [(\omega_{y1,2}^2 - \omega_d^2)^2 + \omega_{y1,2}^2 \omega_d^2 / Q_{y1,2}^2]} e^{-\frac{\omega_{y1,2}}{2Q_{y1,2}} t} \times \sin\left(\sqrt{1 - 1/4Q_{y1,2}^2} \omega_{y1,2} t\right) \quad (3)$$

where $\varphi_{x2} = -tg^{-1}\left(\frac{\omega_{x2} \omega_d}{Q_{x2}(\omega_{x2}^2 - \omega_d^2)}\right)$, $F_c = \frac{-2\Omega_z \omega_d F_d}{m_x \sqrt{(\omega_{x2}^2 - \omega_d^2)^2 + \omega_{x2}^2 \omega_d^2 / Q_{x2}^2}}$, $\varphi_{y1,2} = -tg^{-1}\left(\frac{\omega_{y1,2} \omega_d}{Q_{y1,2}(\omega_{y1,2}^2 - \omega_d^2)}\right)$.

The above Equations indicate that the movement of drive and sensing modes are the compound motion of stable vibration and attenuation vibration. Since drive mode closed-loop is employed, drive mode is stimulated with stable amplitude ($\omega_d = \omega_{x2}$). Then (2) can be simplified as [5]:

$$x(t) = \frac{F_d Q_{x2}}{m_x \omega_d^2} \cos(\omega_d t) = A_x \cos(\omega_d t) \quad (4)$$

The sensing in-phase and anti-phase modes movement Equation can be got from (3):

$$y_{1,2}(t) = \frac{-2\Omega_z F_d Q_{x2} \sin(\omega_d t)}{m_x \omega_d \sqrt{(\omega_{y1,2}^2 - \omega_d^2)^2 + \omega_{y1,2}^2 \omega_d^2 / Q_{y1,2}^2}} = A_{y1,2} \sin(\omega_d t) \quad (5)$$

Then, the mechanical sensitivity can be expressed as:

$$S_{me} = \frac{A_{y1} + A_{y2}}{\Omega_z} \approx \frac{-F_d Q_{x2}}{m_x \omega_d^2} \left(\frac{1}{\omega_{y1} - \omega_{x2}} + \frac{1}{\omega_{y2} - \omega_{x2}} \right) = -A_x \left(\frac{1}{\Delta\omega_1} + \frac{1}{\Delta\omega_2} \right) \quad (6)$$

The mechanical sensitivity of dual-mass sensing mode coupled structure is determined by vibration amplitude of drive mode and frequency differences between drive working mode and sensing modes (including the 2nd and the 3rd modes). Furthermore, the one near the 4th mode is the dominant element. Therefore, the sensing anti-phase mode determines the gyro structure mechanical sensitivity. The schematic diagram of gyro sensing mode is shown in Fig. 3. $G_{inphase}$ and $G_{anphase}$ are transform functions of in-phase and anti-phase sensing modes; K_{inyv} and K_{anyv} are displace-voltage transform parameters of sensing in-phase and anti-phase modes; K_{pre} is the pre amplifier; V_{stotal} is sensing mode output, and $G_{sV/F}$ can be expressed as:

$$G_{sV/F} = (G_{inphase} K_{inyv} + G_{anphase} K_{anyv}) K_{pre} \quad (7)$$

where $G_{inphase} = \frac{1}{m_y} \frac{1}{s^2 + \frac{\omega_{y1}^2}{Q_{y1}^2} s + \omega_{y1}^2}$ is the sensing in-phase mode and $G_{anphase} = \frac{1}{m_y} \frac{1}{s^2 + \frac{\omega_{y2}^2}{Q_{y2}^2} s + \omega_{y2}^2}$ is sensing anti-phase mode.

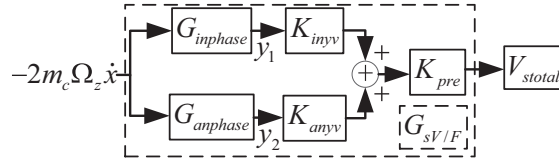


Fig. 3. Schematic diagram of sensing mode real working mode.

2.2. Force rebalancing combs stimulation method (FRCSM)

The force rebalancing combs are slide-film form (does not vary ω_{y1} and ω_{y2}). And they are arranged to generate electrostatic force and rebalance the Coriolis force applied on sense frame. The movement of sensing frame is restricted, which improves the dynamic performance of gyro. Therefore, Coriolis simulation signal is designed to be produced through force rebalancing combs, and this method can be further applied to scale factor and bandwidth tests. The FRCSM schematic diagram is shown in Fig. 4, and the equivalent input angular rate of V_{Tes} is:

$$\Omega_{VTes} = \frac{K_{FBy} V_{Tes} V_{dac}}{2m_c A_x \omega_d} \quad (8)$$

where K_{FBy} is voltage-force interface transform coefficient of force rebalances combs; V_{dac} is modulate signal amplitude, which is picked up after 90 degree shifter in drive loop and is considered to be constant when gyro works. K_{FBy} can be got either from the calculation of structure parameter or turntable test, and it is determined by force rebalancing combs number, parameters and feedback direct voltage V_{FDC} .

2.3. Sensing mode verification in sense open-loop

The gyro control and detection system is shown in Fig. 5. In drive loop, the drive frame displacement $x(t)$ is detected by drive sensing combs and picked up by differential amplifier ①. Then, the signal phase is delayed by 90° (through ②) to satisfy the phase requirement of AC drive signal $V_{dac} \sin(\omega_d t)$. After that, $V_{dac} \sin(\omega_d t)$ is processed by a full-wave rectifier ③ and a low pass filter ④. Afterwards, V_{dac} is compared (in ⑤) with the reference voltage V_{ref} ⑥. Next, drive PI controller ⑦ generates the control signal, which is modulated by $V_{dac} \sin(\omega_d t)$, and then the signal is superposed (through ⑩) by V_{DC} ⑨ to stimulation drive mode.

The sensing system employs a closed-loop, which utilises the same interface as drive circuit. Firstly, the left and right masses' sensing signals are detected separately with differential detection amplifier ⑪. And the output signals are processed by second differential amplifier ⑫ to generate signal V_{stotal} . Then, V_{stotal} is demodulated by signal $V_{dac} \sin(\omega_d t)$ (in ⑬). After that, the demodulated signal V_{dem} passes through the low pass filter ⑭, so, the sensing mode's movement signal V_{Oopen} can be got. For sense closed-loop ("pink" section in Fig. 5), V_{Oopen} is first sent in PIPLC ⑮ to calculate the control signal superposed (through ⑯) with test signal V_{Tes} ⑰. Then the signal is modulated with $V_{dac} \sin(\omega_d t)$ (in ⑱). Finally, DC voltage V_{FDC} ⑲ is superposed with the modulated signal in ⑲ to generate the feedback signal.

In sensing loop, the force rebalancing combs can be considered as sensing combs (they are with same slide-film structure) and can be designed with parallel connection to improve sensing combs' number. But in this section, we want to verify the real working state of sensing mode and draw its Bode map with FRCSM, so the feedback loop is cut after PIPLC and the force rebalancing combs are utilized to generate Coriolis simulation force with V_{Tes} .

The system diagram of sense open loop is shown in Fig. 4, and the Equations below can be got from the figure:

$$F_c(t) = 2\Omega_z(t) m_y A_x \omega_d \sin(\omega_d t) \quad (9)$$

$$F_{yf}(t) = K_{FBy} V_{Tes}(t) V_{dac} \sin(\omega_d t) \quad (10)$$

$$F_{ct}(t) = F_c(t) + F_{yf}(t) \quad (11)$$

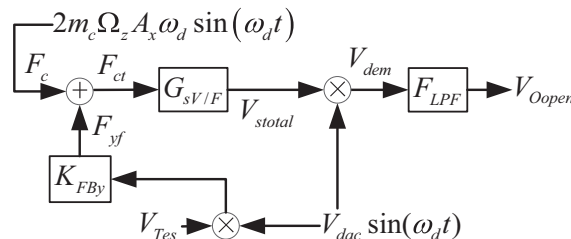


Fig. 4. FRCSM schematic in sensing open loop.

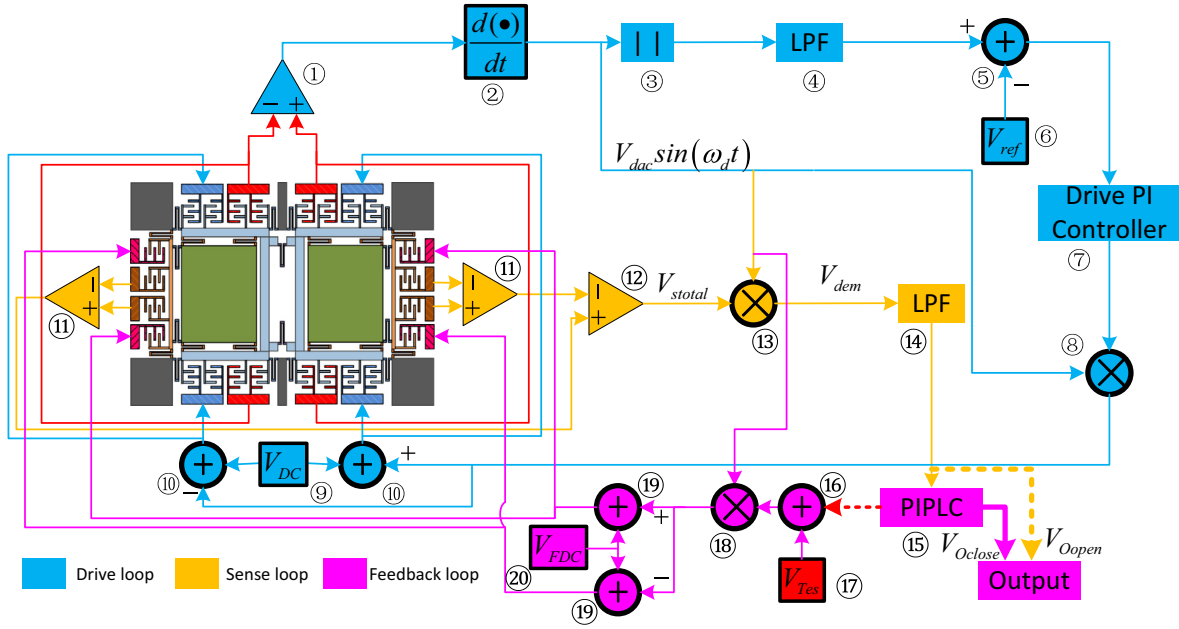


Fig. 5. Gyro system schematic diagram.

After Laplace transformation, we can get:

$$F_{ct}(s) = A_x \omega_d m_c [\Omega_z(s - j\omega_d) + \Omega_z(s + j\omega_d)] + \frac{K_{FBy} V_{dac} [V_{Tes}(s - j\omega_d) + V_{Tes}(s + j\omega_d)]}{2} \quad (12)$$

Then, demodulator output signal V_{dem} is:

$$\begin{aligned} V_{dem}(s) = & \frac{A_x \omega_d V_{dac} K_{pre}}{2} \left\{ \left(\frac{[\Omega_z(s) + \Omega_z(s + 2j\omega_d)] K_{inyv}}{(s + j\omega_d)^2 + \frac{\omega_{y1}}{Q_{y1}}(s + j\omega_d) + \omega_{y1}^2} + \frac{[\Omega_z(s) + \Omega_z(s + 2j\omega_d)] K_{anyv}}{(s + j\omega_d)^2 + \frac{\omega_{y2}}{Q_{y2}}(s + j\omega_d) + \omega_{y2}^2} \right) \right. \\ & + \left. \left(\frac{[\Omega_z(s - 2j\omega_d) + \Omega_z(s)] K_{inyv}}{(s - j\omega_d)^2 + \frac{\omega_{y1}}{Q_{y1}}(s - j\omega_d) + \omega_{y1}^2} + \frac{[\Omega_z(s - 2j\omega_d) + \Omega_z(s)] K_{anyv}}{(s - j\omega_d)^2 + \frac{\omega_{y2}}{Q_{y2}}(s - j\omega_d) + \omega_{y2}^2} \right) \right\} \\ & + \frac{K_{FBy} V_{dac}^2 K_{pre}}{4m_y} \left\{ \left(\frac{[V_{Tes}(s) + V_{Tes}(s + 2j\omega_d)] K_{inyv}}{(s + j\omega_d)^2 + \frac{\omega_{y1}}{Q_{y1}}(s + j\omega_d) + \omega_{y1}^2} + \frac{[V_{Tes}(s) + V_{Tes}(s + 2j\omega_d)] K_{anyv}}{(s + j\omega_d)^2 + \frac{\omega_{y2}}{Q_{y2}}(s + j\omega_d) + \omega_{y2}^2} \right) \right. \\ & + \left. \left(\frac{[V_{Tes}(s - 2j\omega_d) + V_{Tes}(s)] K_{inyv}}{(s - j\omega_d)^2 + \frac{\omega_{y1}}{Q_{y1}}(s - j\omega_d) + \omega_{y1}^2} + \frac{[V_{Tes}(s - 2j\omega_d) + V_{Tes}(s)] K_{anyv}}{(s - j\omega_d)^2 + \frac{\omega_{y2}}{Q_{y2}}(s - j\omega_d) + \omega_{y2}^2} \right) \right\} \end{aligned} \quad (13)$$

After low pass filter F_{LPF} , the high frequency component ($2\omega_d$) is restrained and the output signal is:

$$\begin{aligned} V_{Open}(s) = & K_{pre} \left[\frac{A_x \omega_d V_{dac} \Omega_z(s) F_{LPF}(s)}{2} + \frac{K_{FBy} V_{dac}^2 V_{Tes}(s) F_{LPF}(s)}{4m_y} \right] \\ & \times \left[\frac{K_{inyv} (s^2 + \frac{\omega_{y1}}{Q_{y1}} s + \omega_{y1}^2 - \omega_d^2)}{(s^2 + \frac{\omega_{y1}}{Q_{y1}} s + \omega_{y1}^2 - \omega_d^2)^2 + (2s\omega_d + \frac{\omega_{y1}}{Q_{y1}} \omega_d)^2} + \frac{K_{anyv} (s^2 + \frac{\omega_{y2}}{Q_{y2}} s + \omega_{y2}^2 - \omega_d^2)}{(s^2 + \frac{\omega_{y2}}{Q_{y2}} s + \omega_{y2}^2 - \omega_d^2)^2 + (2s\omega_d + \frac{\omega_{y2}}{Q_{y2}} \omega_d)^2} \right] \end{aligned} \quad (14)$$

then, let:

$$G_{se}(s) = \frac{K_{inyv} (s^2 + \frac{\omega_{y1}}{Q_{y1}} s + \omega_{y1}^2 - \omega_d^2)}{(s^2 + \frac{\omega_{y1}}{Q_{y1}} s + \omega_{y1}^2 - \omega_d^2)^2 + (2s\omega_d + \frac{\omega_{y1}}{Q_{y1}} \omega_d)^2} + \frac{K_{anyv} (s^2 + \frac{\omega_{y2}}{Q_{y2}} s + \omega_{y2}^2 - \omega_d^2)}{(s^2 + \frac{\omega_{y2}}{Q_{y2}} s + \omega_{y2}^2 - \omega_d^2)^2 + (2s\omega_d + \frac{\omega_{y2}}{Q_{y2}} \omega_d)^2}$$

When input angular rate $\Omega_z = 0$, the open-loop output signal is determined by V_{Tes} and the real sensing mode can be tested. The structure of GY-027# (prototype gyro built by authors' team) is investigated in this paper, and its parameter val-

ues are obtained from structure test as shown in Table 1. By using these parameter values, pole-zero map for sensing mode is shown in Fig. 6. The 4 pairs of conjugate poles of sensing mode can be expressed as:

$$p_{1,2} = -\frac{\omega_{y1}}{2Q_{y1}} + \left(\omega_d \pm \frac{\omega_{y1}}{2} \sqrt{4 - \frac{1}{Q_{y1}^2}} \right) j$$

$$p_{3,4} = -\frac{\omega_{y1}}{2Q_{y1}} - \left(\omega_d \pm \frac{\omega_{y1}}{2} \sqrt{4 - \frac{1}{Q_{y1}^2}} \right) j$$

$$p_{5,6} = -\frac{\omega_{y2}}{2Q_{y2}} + \left(\omega_d \pm \frac{\omega_{y2}}{2} \sqrt{4 - \frac{1}{Q_{y2}^2}} \right) j$$

$$p_{7,8} = -\frac{\omega_{y2}}{2Q_{y2}} - \left(\omega_d \pm \frac{\omega_{y2}}{2} \sqrt{4 - \frac{1}{Q_{y2}^2}} \right) j$$

One pair of conjugate poles produces one resonant peak (across + 3 dB line) in Bode diagram, so the bandwidth is determined by the lowest conjugate poles ($p_{5,6}$ in this work). Input the values in Table 1 to Eq. (14), and it can be got that:

$$|\omega_{y1}^2 - \omega_d^2| \gg \left| \frac{\omega_{y1}}{Q_{y1}} \omega_d \right|, \quad |\omega_{y2}^2 - \omega_d^2| \gg \left| \frac{\omega_{y2}}{Q_{y2}} \omega_d \right|, \quad \frac{K_{inyv}}{\Delta\omega_1} \ll \frac{K_{anyv}}{\Delta\omega_2}$$

when $s = 0$, the static simulation scale factor can be expressed as:

$$\frac{V_{Open}(0)}{V_{Tes}(0)} = \frac{K_{FBy} V_{dac}^2 F_{LPF} K_{anyv} K_{pre}}{8m_y \omega_d \Delta\omega_2} \quad (15)$$

Then, by substituting Eq. (8) into Eq. (15), we get:

Table 1
GY-027# Structure Tested Value.

Parameter	Value
ω_d	$3488.9 \times 2\pi$ rad/s
ω_{y1}	$3360.1 \times 2\pi$ rad/s
ω_{y2}	$3464.1 \times 2\pi$ rad/s
Q_{y1}	1051
Q_{y2}	1224

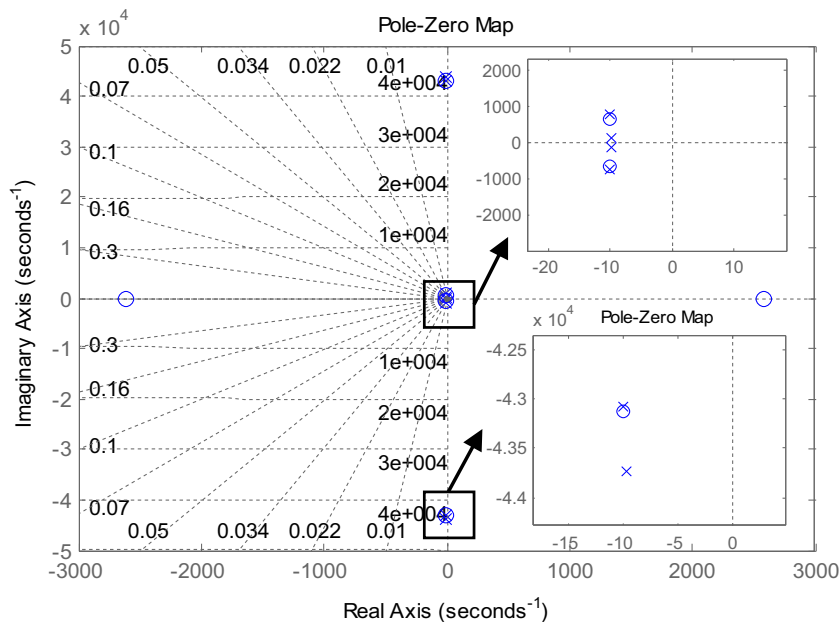


Fig. 6. Pole-Zero map of GY-027# structure sensing mode.

$$\frac{V_{Open}(0)}{\Omega_{VTes}(0)} = \frac{V_{dac}K_{anyv}K_{pre}A_xF_{LPF}}{4\Delta\omega_2} \quad (16)$$

Assuming the bandwidth is ω_b , and $\omega_b \ll \omega_{y2}$, the point $\omega_{open} \leq \omega_b$ exists, and the simulation scale factor at ω_{open} is:

$$\left| \frac{V_{Open}(\omega_{open})}{\Omega_{VTes}(\omega_{open})} \right| = \frac{V_{dac}K_{anyv}K_{pre}A_xF_{LPF}}{4\Delta\omega_2 \left(1 - \frac{\omega_{open}^2}{\Delta\omega_2^2}\right)} \quad (17)$$

The bandwidth is +3 dB point, so we have:

$$\left| \frac{V_{Open}(\omega_b)}{\Omega_{VTes}(\omega_b)} \right| = \sqrt{2} \left| \frac{V_{Open}(0)}{\Omega_{VTes}(0)} \right| \quad (18)$$

By substituting Eq. (16) and (17) into (18), the bandwidth is described in Eq. (19). Then bring the values (in Table 1) into it, the bandwidth of sense open loop is about 13.4 Hz [5].

$$\omega_b = 0.54\Delta\omega_2 \quad (19)$$

Fig. 7 shows the Bode Diagram for sensing real working mode within 200 Hz frequency range. The blue state line is the simulation line in Simulink software and the red dot line with stars is FRCSM test curve. The cut off frequency of LPF is over 500 Hz and does not influence bandwidth characteristic within the 200 Hz range.

The key points parameters in Fig. 8 is illustrated in Table 2. “DC” point means that the equivalent input angular rate V_{Tes} is constant value; +3 dB point is bandwidth restriction point (as discussed in [5]); A (frequency is $\Delta\omega_2$) and C (frequency is $\Delta\omega_1$) peak points are generated by $p_{5,6}$ and $p_{1,2}$ respectively; B valley point ($\Delta\omega_B$) is caused by conjugate zeros shown in

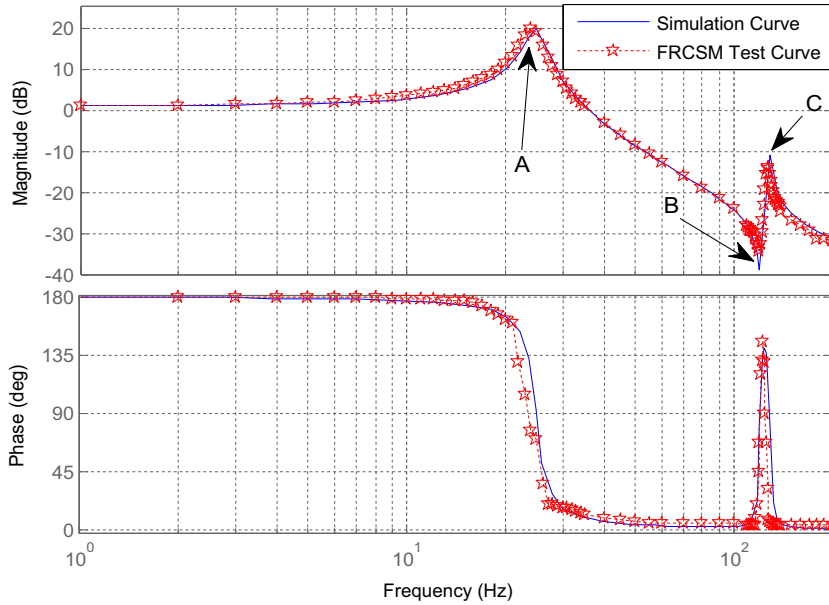


Fig. 7. Simulation and FRCSM test results of GY-027# sensing real working mode Bode Diagram.

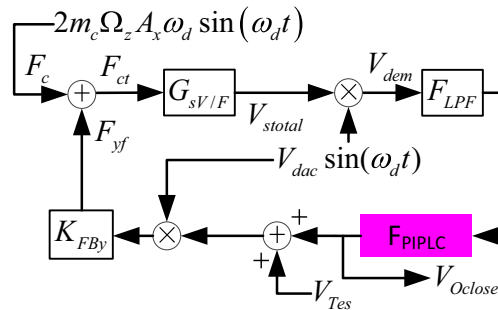


Fig. 8. Sensing closed-loop schematic.

Table 2

GY-027# Structure Bode diagram key points values.

Simulation			FRCSM test	
Point	Frequency (Hz)	Magnitude (dB)	Frequency (Hz)	Magnitude (dB)
DC	0	1.15	0	1.07
+3 dB	12.9	4.15	13	4.11
A	24.8	19.5	24	19.7
B	120	−39.3	120	−34.4
C	128	−11.4	128	−13.9

top-right small schematic of Fig. 6. The bandwidth obtained from the simulation curve is 12.9 Hz and from FRCSM test curve is 13 Hz (according to literature [23], the bandwidth is A, because of the -90° phase shift), which verifies the theory calculation result in Eq. (18). The frequency values of A and C peak points identify the values in Table 1. In addition, the FRCSM test curve matches simulation curve well and proves the theory analysis conclusion proposed in Section 2.1.

It can be got obviously from Eqs. (6) and (19) that the gyro mechanical sensitivity and bandwidth in sense open loop are conflicting with each other. So an efficient bandwidth expanding technology should be researched to break this bottleneck.

3. Sensing closed-loop design and bandwidth expanding

3.1. Sensing closed-loop analysis and design

Sensing closed-loop control method provides electrostatic force to rebalance the Coriolis force applied on sensing mode, which is one of the most effective ways to improve gyro dynamic performance. When sensing closed-loop works, the sensing frame's displacement is restricted and the Coriolis force is transformed into electronic signal directly. And it also avoids the nonlinearity of sensing mode displacement. Meanwhile, closed loop provides better anti-vibration and anti-shock characteristics to the gyroscope. The sensing closed-loop schematic is shown in Fig. 8, where the real input angular rate $\Omega_z = 0^\circ/\text{s}$ and the simulation angular rate V_{Tes} is employed to test the closed system frequency response. From Fig. 8, the Equations can be got:

$$F_{yf}(t) = K_{FBy}[V_{\text{Oclose}}(t) + V_{\text{Tes}}(t)]V_{\text{dac}} \sin(\omega_d t) \quad (20)$$

$$V_{\text{Oclose}}(s) = V_{\text{dem}}(s)F_{LPF}(s)F_{PIPLC}(s) \quad (21)$$

Similarly by using the analysis method mentioned in Section 2.3 and combining Eq. (20) with (21), we have:

$$\left| \frac{V_{\text{Oclose}}(\omega_{\text{open}})}{\Omega_{V_{\text{Tes}}}(\omega_{\text{open}})} \right| = \frac{2m_c A_x \omega_d K_{pre} G_{se} V_{\text{dac}} F_{LPF}(s) F_{PIPLC}(s)}{4m_y - K_{pre} K_{FBy} V_{\text{dac}}^2 G_{se} F_{LPF}(s) F_{PIPLC}(s)} \quad (22)$$

Because $4m_y \ll K_{pre} K_{FBy} V_{\text{dac}}^2 G_{se} F_{LPF}(s) F_{PIPLC}(s)$ within bandwidth range (G_{se} reduces a lot at point B, so bandwidth range is considered before point B), Eq. (22) can be expressed as:

$$\left| \frac{V_{\text{Oclose}}}{\Omega_{V_{\text{Tes}}}} \right| = \frac{2m_c A_x \omega_d}{K_{FBy} V_{\text{dac}}} \quad (23)$$

The above Equation means that the scale factor in closed loop is constant value and is not restricted by resonant peak (A point).

3.2. Proportional integral phase lead controller (PIPLC) design

Generally speaking, the open loop Bode diagram of sensing closed-loop is expected to have following characteristics:

- In low frequency range, a first order pure integral element is configured to achieve enough gain and reduce the steady state error of the system.
- In middle frequency range, the slope of magnitude line is designed to be -20 dB/dec at 0 dB crossing frequency point. The cut off frequency is ω_{cut} , which provides enough phase margin (more than 30°).
- At $\Delta\omega_2$ frequency point (A point), the phase lags 180° acutely, so two first order differential elements are utilized to compensate the system phase before $\Delta\omega_2$. After the phase compensation, the -180° crossing frequency is improved and optimizes the magnitude margin (expected more than 5 dB).
- Since a pair of conjugate zero is at $\Delta\omega_B$, which provides $+20 \text{ dB/dec}$ magnitude curve, cut off frequency ω_{cut} is arranged before $\Delta\omega_B$.
- In high frequency range, the magnitude curve is designed to be -60 dB/dec to reduce magnitude rapidly, which restrains high frequency noise and white noise effectively. F_{LPF} element is second order type and generates -40 dB/dec , and a pair of conjugate pole is at $\Delta\omega_1$, providing -20 dB/dec slope.

- f. An inertial element is required to match the phase compensation elements and its frequency should be arranged outside the bandwidth. Meanwhile, the inertial element also provides another -20 dB/dec slope in high frequency range, which is better to restrain high frequency noise.
- g. Temperature compensation module is required to ensure the wide-temperature range characteristic of PIPLC.

So, the PIPLC is expressed as:

$$F_{PIPLC}(s) = k_{pi}(t_{tem}) \frac{s + \omega_{pi1}}{s} \frac{s + \omega_{pi1}}{s + \omega_{pi2}(t_{tem})} \quad (24)$$

According to the analysis, we make $k_{pi} = 32$ (experience value, over high value brings instability), $\omega_{pi1} = 10\pi$ rad/s and $\omega_{pi2} = 400\pi$ rad/s. In addition, the k_{pi} and ω_{pi2} can be adjusted by temperature t_{tem} . The PIPLC circuit diagram is shown in Fig. 9. The transform function can be written as following:

$$F_{PIPLC}(s) = \frac{R_{pi2}R_{pi4}}{(R_{pi1} + R_{pi1t})(R_{pi3} + R_{pi3t})} \frac{\left(s + \frac{1}{R_{pi2}C_{pi1}}\right)}{s} \frac{\left(s + \frac{1}{R_{pi4}C_{pi3}}\right)}{\left(s + \frac{1}{(R_{pi3} + R_{pi3t})C_{pi2}}\right)} \quad (25)$$

Assuming the temperature is room temperature (20°C), the PIPLC module in Eq. (25) is simulated in Simulink software, and the circuit level simulation with parameters of Table 3 is carried out in Multisim software. These two curves are shown in Fig. 10. Obviously, they matches very well, which proves that the circuit and the parameters are feasible.

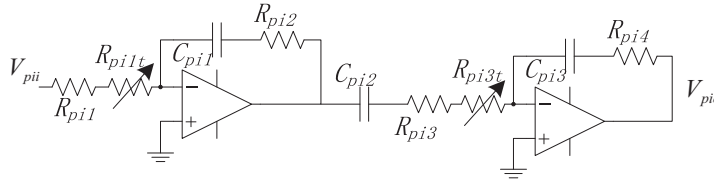


Fig. 9. PIPLC circuit diagram.

Table 3

PIPLC parameter values.

Parameter	Value	Parameter	Value
R_{pi1}	$30\text{k}\Omega$	C_{pi1}	$0.33\mu\text{F}$
R_{pi2}	$100\text{k}\Omega$	C_{pi2}	$0.33\mu\text{F}$
R_{pi3}	1400Ω	C_{pi3}	$0.33\mu\text{F}$
R_{pi4}	$100\text{k}\Omega$	R_{pi1t}	$100\,000 + k_1 t_{tem}\Omega^a$
		R_{pi3t}	$1\,000 + k_3 t_{tem}\Omega^b$

^a k_1 is the temperature coefficient of R_{pi1t} ;

^b k_3 is the temperature coefficient of R_{pi3t} ;

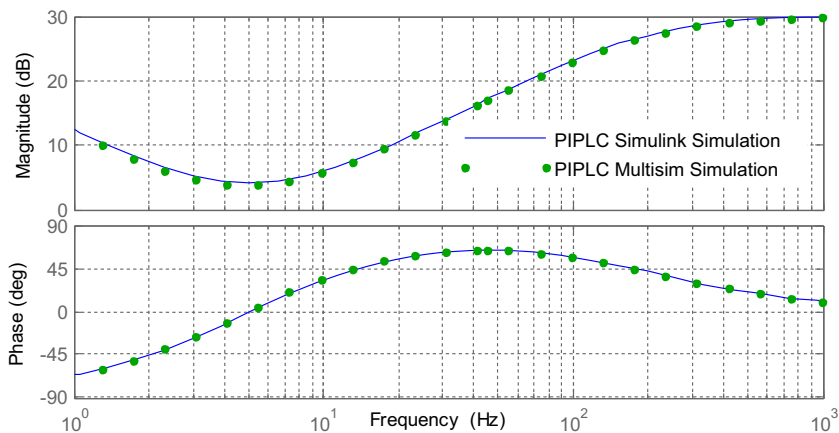


Fig. 10. PIPLC system and circuit level simulation curves.

The open-loop Bode Diagram of the sensing closed-loop is simulated in Simulink software and shown in Fig. 11. The figure indicates that the minimum phase margin of the loop is 34.6° , and the magnitude margin is 7.21 dB, which satisfy the design requests. The Pole-Zero Map and Nyquist Map of sensing closed-loop are shown in Figs. 12 and 13. The poles distribute in negative side of real axis and the Nyquist curve does not contains $(-1, 0j)$ point. These above two criterions both illustrate the closed system is pretty stable. The Bode Diagram of sensing closed-loop simulation is shown in Fig. 14, whose curves indicates that the bandwidth of the gyro is 100 Hz, the lowest point within the bandwidth range is -13.8 dB, the DC magnitude is -12.3 dB, and the highest point is -10.4 dB. The resonant peak A is compensated, and the new bandwidth bottleneck point is valley B. Therefore, one of the best methods to expand the bandwidth under this condition is to enlarge the frequency difference between ω_{y1} and ω_{y2} .

3.3. Bandwidth analysis and simulation in full temperature range

The silicon structure's parameters are influenced seriously by temperature, including resonant frequency, quality factor and so on [4]. So the variation of pole-zero map of the structure during the wide-temperature range (from -40°C to 60°C in

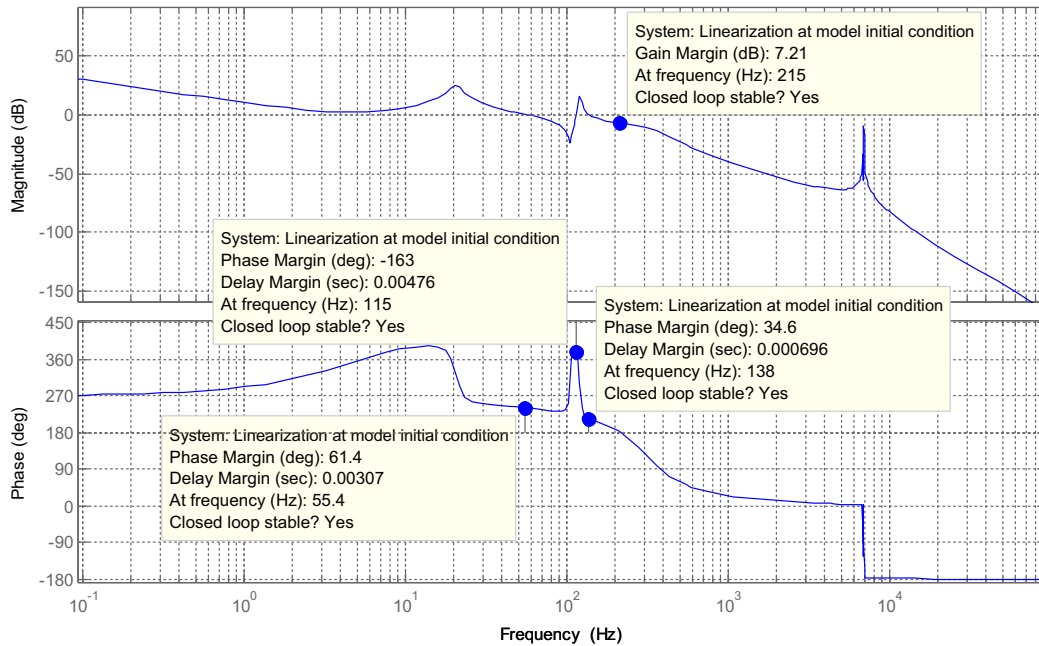


Fig. 11. Open loop Bode Diagram of sense close loop.

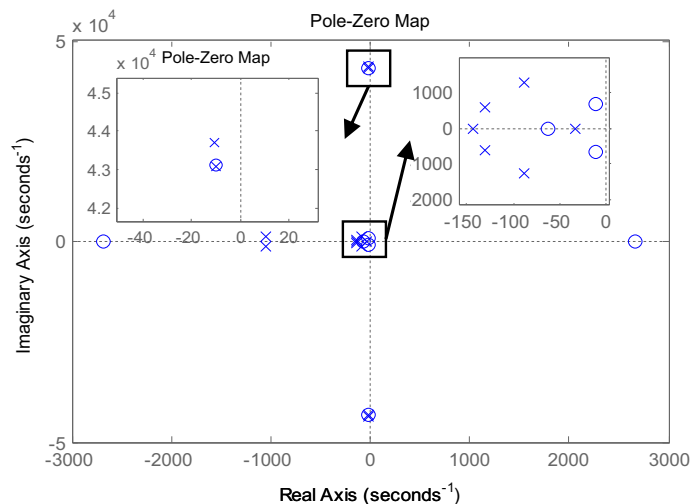


Fig. 12. Pole-Zero Map of sense close loop.

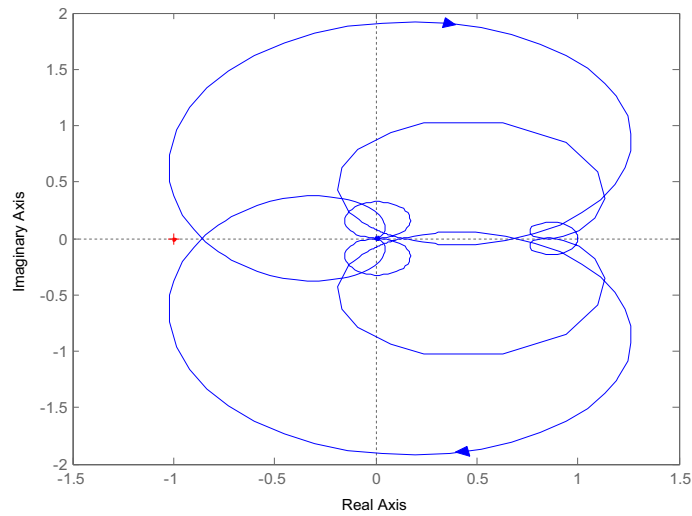


Fig. 13. Nyquist Map of sense close loop.

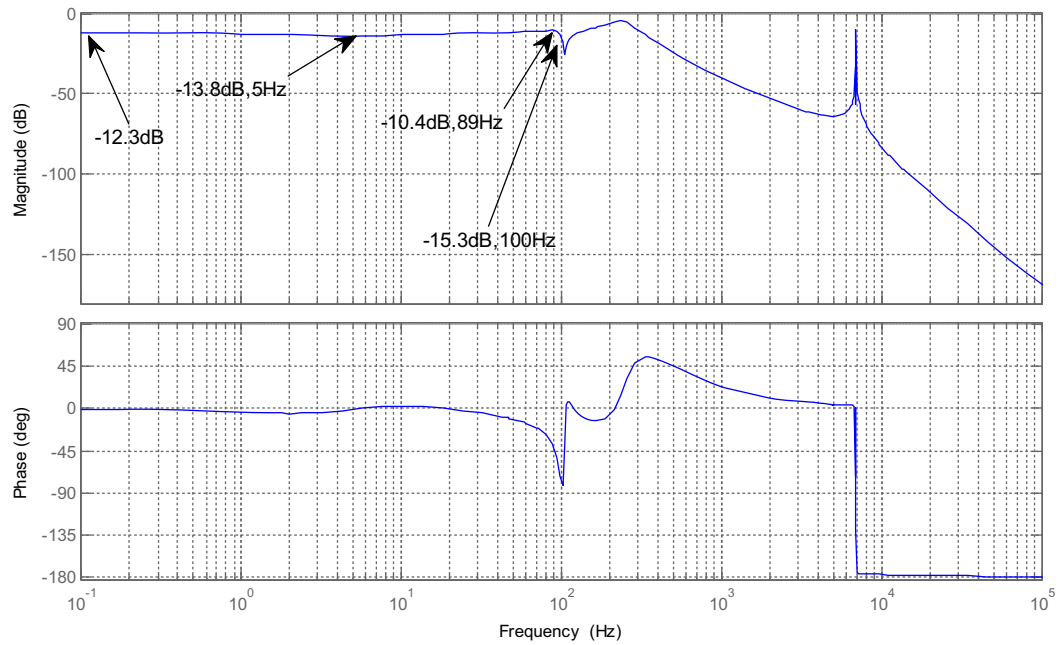


Fig. 14. Sense close loop simulation Bode Diagram.

Table 4
GY-027# Structure Parameters During The Full Temperature Range.

°C	$\omega_d/2\pi(\text{Hz})$	$\omega_{y2}/2\pi(\text{Hz})$	$\Delta\omega_2/2\pi(\text{Hz})$	Q_{y2}
-40	3494.7	3470.8	23.9	1559
-30	3494.2	3470.1	24.1	1495
-20	3493.1	3468.9	24.2	1426
-10	3492.1	3467.9	24.2	1362
0	3491.5	3467.0	24.5	1315
10	3490.1	3465.5	24.6	1275
20	3488.9	3464.1	24.8	1224
30	3488.4	3463.6	24.8	1199
40	3487.5	3462.6	24.9	1151
50	3486.2	3461.3	24.9	1130
60	3485.7	3460.7	25.0	1122

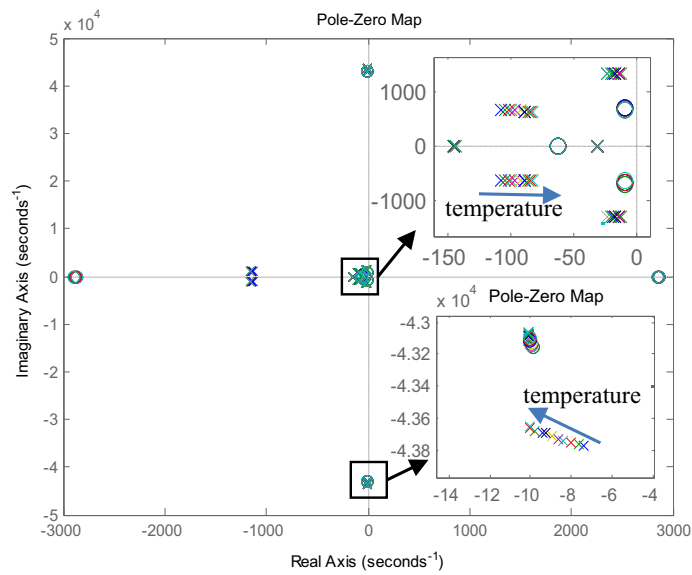


Fig. 15. Sensing closed-loop simulation Pole-Zero Map in full temperature range.

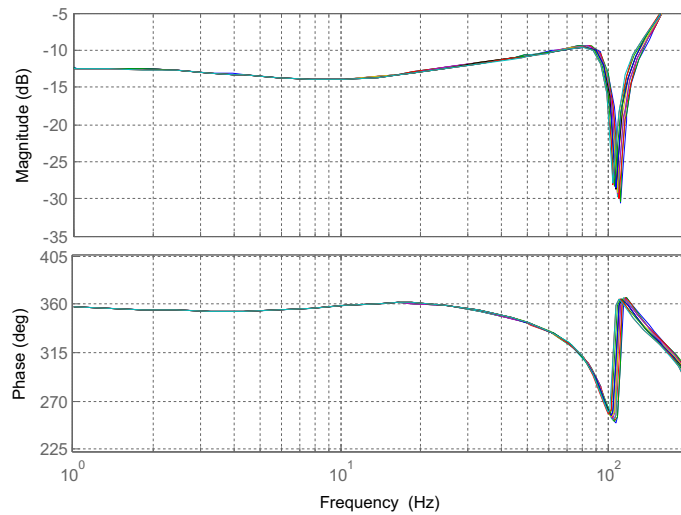


Fig. 16. Sensing closed-loop simulation Bode Diagram in full temperature range.

Table 5

Simulation results Of GY-027# Bode Diagram in full temperature range.

Temperature(°C)	DC magnitude (dB)	Lowest point in bandwidth		Highest point in bandwidth		Bandwidth [23] (Hz)
		Frequency (Hz)	Magnitude(dB)	Frequency (Hz)	Magnitude(dB)	
−40	−12.393	7.80	−13.890	84.0	−9.449	103
−30	−12.395	7.79	−13.905	84.2	−9.450	103
−20	−12.397	7.79	−13.915	84.1	−9.471	102
−10	−12.401	7.79	−13.916	83.8	−9.512	101
0	−12.403	7.77	−13.940	84.1	−9.511	101
10	−12.407	7.76	−13.950	83.6	−9.533	101
20	−12.410	7.75	−13.965	82.8	−9.550	100
30	−12.412	7.75	−13.965	82.4	−9.561	99.7
40	−12.414	7.75	−13.974	81.8	−9.592	99.2
50	−12.417	7.75	−13.976	80.9	−9.621	98.7
60	−12.418	7.75	−13.985	80.5	−9.628	98.2

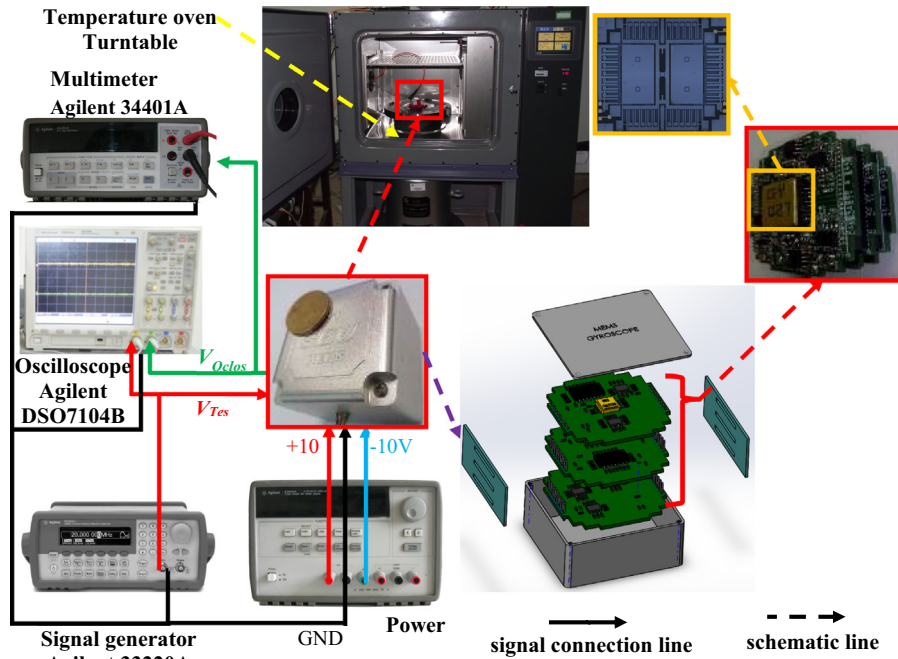


Fig. 17. Photos of test equipments and gyroscope.

this paper) makes the peak and valley position constantly changing. The mechanical parameters of GY-027# structure during the wide-temperature range are tested and shown in Table 4. The bandwidth restriction element is peak A, and we focus on $\Delta\omega_2$ frequency and Q_{y2} values. The simulation results of sensing closed-loop during wide-temperature range are shown in Fig. 15 (Pole-Zero Map) and Fig. 16 (closed loop Bode Diagram in 200 Hz). In Fig. 15, it is obvious that no pole is in positive side of real axis, proving that the closed loop is stable in wide-temperature range.

The simulation results in Fig. 16 are shown in Table 5. The bandwidth within wide-temperature range changes about 5% totally, and the bandwidth is better (103 Hz) in low temperature (-40°C) and worse (98.2 Hz) in high temperature (60°C).

4. Tests

4.1. Test equipment and gyro package

The experiments are arranged to verify the content in Chapter III. The test equipment and the sample gyro GY-027# is shown in Fig. 17. The dimensions of gyro is $46 \times 46 \times 36 \text{ mm}^3$. The monitoring circuit is arranged in three PCBs, whose electronic signal and mechanical structure connect with each other through metal pins. Firstly, these PCBs are packaged by rubber pad, which can protect the PCBs and the structure chip from shock and vibration. Then they are put into the metal shell connected with “GND” signal, which provides the electromagnetism shield. The first piece of PCBs is connected with the structure chip, being the interface and processing the weak signals. The second piece of PCBs is the drive closed loop, and the last piece is the sensing closed-loop with PIPLC circuit.

The test equipment includes the power (Agilent E3631A) providing $\pm 10 \text{ V}$ DC voltage and GND, the signal generator (Agilent 33220A) producing V_{Tes} , the oscilloscope (Agilent DSO7104B) and multimeter (Agilent 34401A), which are used to observe and measure the signal's phase and amplitude; the temperature oven providing wide-temperature range environment and turn table test the real bandwidth of the gyro.

4.2. Room temperature bandwidth experiments

The gyro is fixed on the turntable and tested under room temperature (about 20°C) with FRCSM. More specifically, the employed method is step-by-step test and step length is 1 Hz. Firstly, the result is shown as Fig. 18 with red stars¹, where the bandwidth is about 104 Hz (as the simulation value is 100 Hz in Fig. 14) [23]. Since the scale factor can be adjusted with the output level amplifier, the -3 dB point is the key, not the absolute value of the magnitude. After the turntable test is done, since

¹ For interpretation of color in Figs. 18 and 19, the reader is referred to the web version of this article.

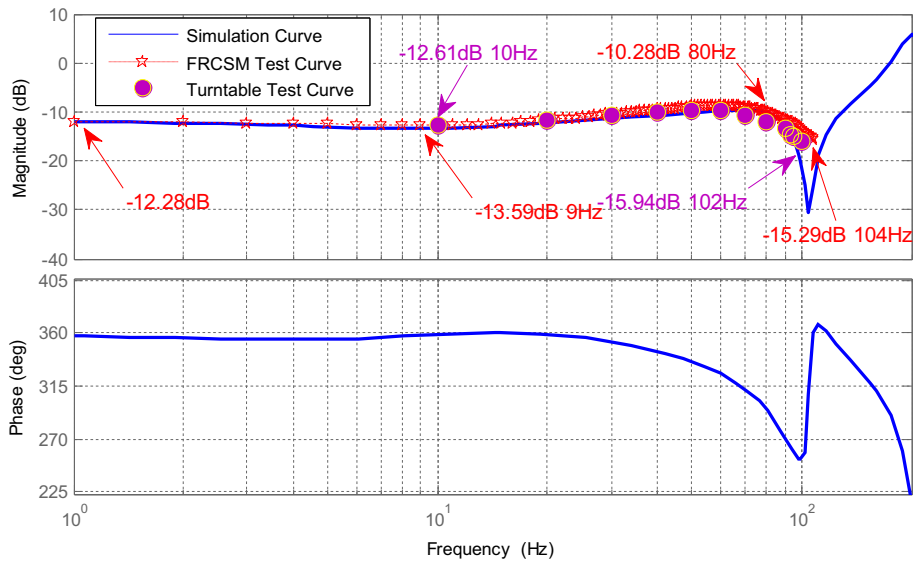


Fig. 18. Room temperature bandwidth test results.

the turntable's swing frequency value is hard to get accurately, we mainly focus on the bandwidth, not each frequency point's value. Within the bandwidth range, the step-by-step test (step length is 10 Hz) is carried out, and the bandwidth is found to be 102 Hz, which verifies the FRCSM result.

4.3. Wide-temperature range bandwidth experiments

Firstly, the temperature oven is cooled down to -40°C . After it reaches -40°C , we keep the temperature for one hour to make sure the temperature distributes equally inside and outside the gyro's metal shell. By utilizing 1 Hz step-by-step test in FRCSM test, its result curve is shown in Fig. 19 (red stars). In addition, the turntable test result is shown with pink dots. The gyro bandwidth values of FRCSM and turntable test are 108 Hz and 107 Hz respectively, which proves the simulation result (103 Hz) well. Then, the temperature is warmed up to 60°C and keep the temperature one hour. Next, the gyro bandwidth is tested with same method. Finally, the bandwidth of FRCSM test is 98 Hz, and the bandwidth of turntable test is 97 Hz. The simulation result shown in Fig. 20 is 98 Hz. Therefore, the wide-temperature range test results verify that the high

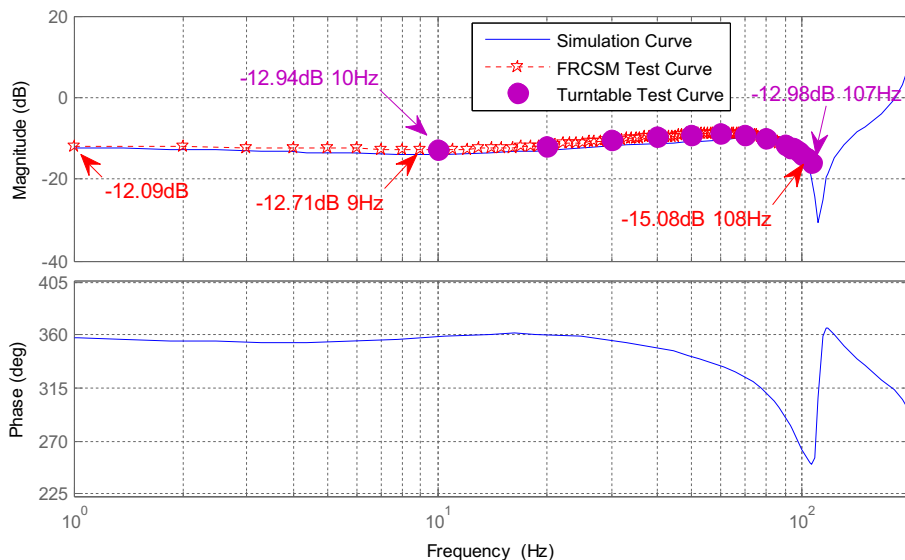


Fig. 19. -40°C bandwidth test results.

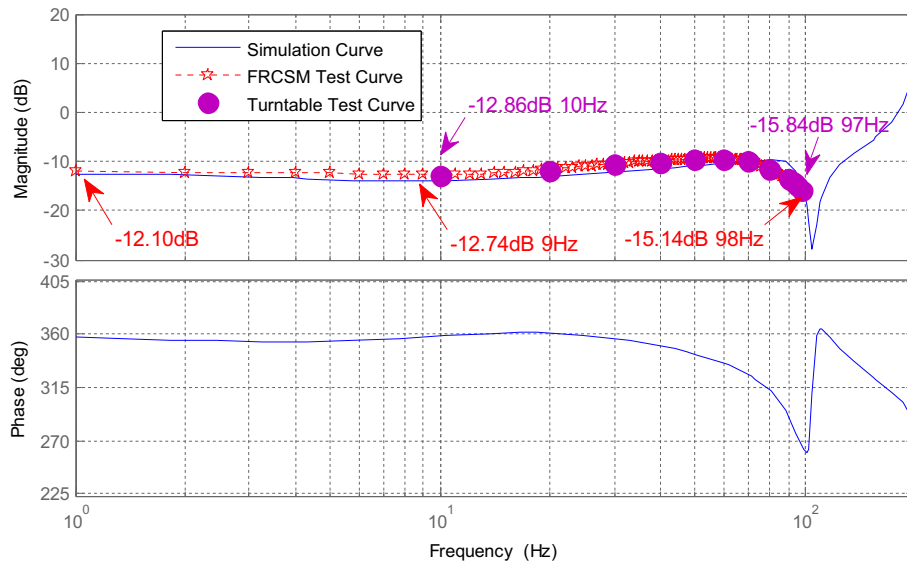


Fig. 20. 60 °C bandwidth test results.

temperature brings low bandwidth and the cooler environment makes gyro have a better bandwidth performance, which agrees with theory analysis.

5. Conclusion and discussion

This paper focuses on the real working state of sensing mode coupling dual-mass MEMS gyroscope, and indicates that the sensing real working mode is formed by sensing in-phase and anti-phase modes. The mechanical sensitivity of sensing mode is governed by the smaller resonant frequency difference between sensing and drive modes ($\min\{\Delta\omega_1, \Delta\omega_2\}$), and the gyro's mechanical bandwidth is also determined by $\min\{\Delta\omega_1, \Delta\omega_2\}$. Therefore, the sensitivity conflicts with gyro bandwidth within sensing open-loop. The force rebalancing combs stimulation method (FRCSM) is introduced to simplify the gyro's dynamic test process, which has higher sensitivity and precision than turntable test method. In order to improve the dynamic performance of gyro, the resonant frequency of sensing anti-phase mode is designed to near drive mode frequency. The frequency gaps are $\Delta\omega_2 = 24.8 * 2\pi$ rad/s and $\Delta\omega_1 = 128.8 * 2\pi$ rad/s, and the bandwidth of sense open loop is about 13 Hz. The proportional integral phase lead controller (PIPLC) is designed to expand the gyro's closed-loop bandwidth. The magnitude and phase of the system are 7.21 dB and 34.6° respectively. The controller and the system are simulated in Simulink software and the results show that the bandwidth is stable during the wide-temperature range (from -40°C to 60°C): 103 Hz @ -40°C , 98.2 Hz @ 60°C . The experiments prove that the bandwidth is expanded from 13 Hz to 104 Hz (with FRCSM) in room temperature, to 102 Hz (with turntable method) in room temperature, to 107 Hz @ -40°C (with turntable method) and to 97 Hz @ 60°C (with turntable method). And the results verify the theory analysis and simulation results. The new bottleneck of the closed loop bandwidth is the valley generated by the pair of conjugate zeros, which is formed by the superposition of in-phase and anti-phase sensing mode. What's more, it is proved that large difference between $\Delta\omega_1$ and $\Delta\omega_2$ is better for bandwidth expanding (see Table 6).

Table 6

GY-027# Gyro Bandwidth simulation and experiment results conclusion.

Parameter	Open loop	Closed loop
Simulation bandwidth @ 20°C (Hz)	12.9	100
FRCSM test bandwidth @ 20°C (Hz)	13	104
Turntable test bandwidth @ 20°C (Hz)	–	102
Simulation bandwidth @ -40°C (Hz)	–	103
FRCSM test bandwidth @ -40°C (Hz)	–	108
Turntable test bandwidth @ -40°C (Hz)	–	107
Simulation bandwidth @ 60°C (Hz)	–	98.2
FRCSM test bandwidth @ 60°C (Hz)	–	98
Turntable test bandwidth @ 60°C (Hz)	–	97
Bottleneck element	A point	B point

Acknowledgments

This study was supported by National Natural Science Foundation of China (No. 61603353), Science and Technology on Electronic Test and Measurement Laboratory Fund (No. ZDSYSJ2015004) and Shanxi Scholarship Council of China (No. 2016-083). Huiliang Cao and Xingling Shao contributed equally to this work.

References

- [1] Y. Xu, X. Chen, Y. Wang, Two-mode navigation method for low-cost IMU-based indoor pedestrian navigation, *Simulat. Trans. Soc. Model. Simulat. Int.* 92 (9) (2016) 839–848.
- [2] C. Shen, R. Song, J. Li, X. Zhang, J. Tang, Y. Shi, J. Liu, H. Cao, Temperature drift modeling of MEMS gyroscope based on genetic-Elman neural network, *Mech. Syst. Sig. Proc.* 72–73 (2016) 897–905.
- [3] R. Antonello, R. Oboe, Exploring the potential of MEMS gyroscopes, *IEEE Ind. Electron. Mag.* 6 (1) (Mar. 2012) 14–24.
- [4] H. Cao, H. Li, X. Sheng, S. Wang, B. Yang, L. Huang, A novel temperature compensation method for a MEMS gyroscope oriented on a periphery circuit, *Int. J. Adv. Rob. Syst.* 10 (327) (Sep. 2013) 1–10.
- [5] M. Bao, *Micro Mechanical Transducers Pressure Sensors, Accelerometers and Gyroscopes*, first ed., Elsevier, Amsterdam, The Netherlands, 2000.
- [6] M. Zaman, A. Sharma, Z. Hao, F. Ayazi, A mode-matched silicon-yaw tuning-fork gyroscope with subdegree-per-hour Allan deviation bias instability, *J. Microelectromech. Syst.* 17 (6) (Dec. 2008) 1526–1536.
- [7] C.D. Ezekwe, B.E. Boser, A mode-matching $\Sigma\Delta$ closed-loop vibratory gyroscope readout interface with a $0.004^\circ/\text{s}/\sqrt{\text{Hz}}$ noise floor over a 50Hz band, *IEEE J. Sol.-State Circ.* 43 (12) (Dec. 2008) 3039–3048.
- [8] S. Sonmezoglu, S.E. Alper, T. Akin, An automatically mode-matched MEMS gyroscope with wide and tunable bandwidth, *J. Microelectromech. Syst.* 23 (2) (2014) 284–297.
- [9] W. Sung, S. Sung, J.G. Lee, T. Kang, Design and performance test of a MEMS vibratory gyroscope with a novel AGC force rebalance control, *J. Micromech. Microeng.* 17 (10) (2007) 1939–1948.
- [10] J. Cui, Z. Guo, Q. Zhao, Z. Yang, Y. Hao, G. Yan, Force rebalance controller synthesis for a micromachined vibratory gyroscope based on sensitivity margin specifications, *J. Microelectromech. Syst.* 20 (6) (2011) 1382–1394.
- [11] H. Cao, H. Li, Investigation of a vacuum packaged MEMS gyroscope architecture's temperature robustness, *Int. J. Appl. Electromagnet Mech* 41 (4) (2013) 495–506.
- [12] C. He, Q. Zhao, Y. Liu, Z. Yang, G. Yan, Closed loop control design for the sensing mode of micromachined vibratory gyroscope, *Sci. China Tech. Sci.* 56 (5) (2013) 1112–1118.
- [13] A. Alshehri, M. Kraft, P. Gardonio, Two-mass MEMS velocity sensor: internal feedback loop design, *IEEE Sens. J.* 13 (3) (2013) 1003–1011.
- [14] A.A. Trusov, A.R. Schofield, A.M. Shkel, Study of substrate energy dissipation mechanism in in-phase and anti-phase micromachined vibratory gyroscope, in: *IEEE Sensors Conference*, 2008, pp. 168–171.
- [15] Y. Ni, H. Li, L. Huang, X. Ding, H. Wang, On bandwidth characteristics of tuning fork micro-gyroscope with mechanically coupled sensing mode, *Sensors* 14 (7) (2014) 13024–13045.
- [16] C. Si, G. Han, J. Ning, F. Yang, Bandwidth optimization design of a multi degree of freedom MEMS gyroscope, *Sensors* 13 (8) (2013) 10550–10560.
- [17] C. Acar, A.M. Shkel, An approach for increasing drive-mode bandwidth of MEMS vibratory gyroscopes, *J. Microelectromech. Syst.* 14 (3) (2008) 520–528.
- [18] Z.C. Feng, M. Fan, V. Chellaboina, Adaptive input estimation methods for improving the bandwidth of microgyroscopes, *IEEE Sens. J.* 7 (4) (Apr. 2007) 562–567.
- [19] J. Cui, C. He, Z. Yang, H. Ding, Z. Guo, Y. Hao, G. Yan, Virtual rate-table method for characterization of microgyroscopes, *IEEE Sens. J.* 12 (6) (2012) 2192–2198.
- [20] A. Walther, C.L. Blanc, N. Delorme, et al, Bias contributions in a MEMS tuning fork gyroscope, *J. Microelectromech. Syst.* 22 (2) (2013) 303–308.
- [21] M. Saukski, L. Aaltonen, K.A.I. Halonen, Zero-rate output and quadrature compensation in vibratory MEMS gyroscopes, *IEEE Sens. J.* 7 (12) (2007) 1639–1652.
- [22] H. Cao, H. Li, J. Liu, Y. Shi, J. Tang, C. Shen, An improved interface and noise analysis of a turning fork microgyroscope structure, *Mech. Syst. Sig. Proc.* 70–71 (2016) 1209–1220.
- [23] IEEE Standard Specification Format Guide and Test Procedure for Coriolis Vibratory Gyros, *IEEE Std 1431–2004*, pp. 1–78, Dec. 20 2004.